




Implementation of UV rotational Raman channel to improve aerosol retrievals from multiwavelength lidar

PABLO ORTIZ-AMEZCUA,^{1,2,*}  ANDRÉS ESTEBAN BEDOYA-VELÁSQUEZ,³ JOSE ANTONIO BENAVENT-OLTRA,^{1,2} DANIEL PÉREZ-RAMÍREZ,^{1,2} IGOR VESELOVSKII,⁴ MARIO CASTRO-SANTIAGO,^{1,2} JUAN ANTONIO BRAVO-ARANDA,^{1,2} ANDERSON GUEDES,⁵ JUAN LUIS GUERRERO-RASCADO,^{1,2} AND LUCAS ALADOS-ARBOLEDAS^{1,2}

¹Department of Applied Physics, University of Granada. Granada, Spain

²Andalusian Institute for Earth System Research (IISTA-CEAMA), Granada, Spain

³Sciences Faculty, Department of Physics, Universidad Nacional de Colombia. Medellín, Colombia

⁴General Physics Institute, Moscow, Russia

⁵School of Science and Technology, Universidade Federal do Rio Grande do Norte, Natal, Brazil

*portizamezcu@ugr.es

Abstract: Vibrational Raman effect is widely used in atmospheric lidar systems, but rotational Raman present several advantages. We have implemented a new setup in the ultraviolet branch of an existing multiwavelength lidar system to collect signal from rotational Raman lines of Oxygen and Nitrogen. We showed that, with an appropriate filter wavelength selection, the systematic error introduced in the particle optical properties due to temperature dependence was less than 4%. With this new setup, we have been able to retrieve aerosol extinction and backscatter coefficients profiles at 355 nm with 1-h time resolution during daytime and up to 1-min time resolution during nighttime.

© 2020 Optical Society of America under the terms of the [OSA Open Access Publishing Agreement](#)

1. Introduction

Lidar technique is known to be a robust tool for atmospheric research since it provides vertical profiles of aerosol particles using one or several wavelengths, with very high spatial and temporal resolution. In lidar applications, Raman effect between vibrational energy states of molecules (vibrational Raman, VR) is widely used. In particular, Raman scattering from N₂ and O₂ molecules provides additional information to the elastic scattered lidar signal that makes possible the independent retrieval of particle extinction (α^a) and backscatter (β^a) coefficients [1]. This reduces the errors introduced with Klett-Fernald method for elastic lidars [2,3], since Raman signal constitutes an additional information vector and less assumptions must be taken. Moreover, vertical profiles of particle lidar ratio (LR^a) can be retrieved and used as an indicator of the aerosol type. Another advantage of Raman method is that it can be used to determine the overlap function, an experimental function to correct system alignment and unknown parameters [4].

Lidar systems that are part of lidar networks as EARLINET (European Aerosol Research Lidar Network) [5] or LALINET (Latin America Lidar Network) [6,7] usually measure signals corresponding to VR effect, but there are some disadvantages. The Signal-to Noise Ratio (SNR) is very low for the power of the lasers commonly used, what makes the retrieval of aerosol optical properties quite noisy. In order to increase this SNR, the signals are usually collected during certain integration time, resulting in profiles with temporal resolution of 30-60 min during nighttime. Daytime retrievals are not usually available for VR systems, excepting those with very powerful lasers, e.g. [8]. Furthermore, the significant wavelength shift of the scattered radiation

(30–75 nm) is an important source of uncertainty in α^a and β^a calculation, since the spectral dependence of the radiation has to be assumed [9,10].

The issues of VR can be overcome by measuring at wavelengths corresponding to the pure rotational energy states (rotational Raman, RR) of the considered molecules. These spectral lines present much higher SNR, thus allowing for detection of much less noisy Raman signals. Therefore, they need shorter integration time and the temporal resolution of the obtained profiles can be around 1–5 min during nighttime, as it is shown in the present paper. This technique allows even for daytime retrievals [11,12], and in this paper a temporal resolution of 60 min is obtained for the optical profiles. Another advantage is the significantly smaller wavelength shift for RR (a few nm) than for VR. This means that the assumption needed in Raman inversion method, that particle extinction-related Angström Exponent (AE_α) of particle extinction equals 1, introduces much smaller α^a and β^a uncertainties.

RR measurements have already been used for lidar applications, very often to obtain temperature profiles, e.g. [13–18]. However, when the aim of the lidar measurements is to retrieve α^a and β^a profiles, the temperature dependence of RR lines becomes an issue. This has already been overcome using different approaches, like collecting signals from lines with opposite temperature dependence [15,18]. The approach used in this paper was already presented by Veselovskii et al. [10] for 532 nm and by Haarig et al. [19] for 1064 nm and is based on selecting only a part of the spectrum with low temperature sensitivity. The main advantage of this method is that the implementation of the RR channel can be done with few modifications on an already existing VR lidar.

This paper is disposed as follows: section 2 contains a description of the Raman lidar system where the rotational Raman channel was implemented and the methodology for the retrievals. In section 3, an uncertainty analysis is presented together with a test of signal quality. Results for diurnal and nocturnal retrievals are shown in section 4, and the final summary and conclusions are given in section 5.

2. Instrumental description and methodology

The new channel was implemented in the multiwavelength Raman lidar system MULHACEN, based on a LR331D400 manufactured by Raymetrics Inc. (with several upgrades). This system is located at Granada station (37.16°N, 3.61°W, 680 m above sea level) and is part of EARLINET-ACTRIS (Aerosol, Clouds and Trace Gases Research Infrastructure). It has monostatic biaxial alignment pointing vertically to the zenith. The light source is a Nd:YAG pulsed laser (Quantel CFR Series) with fundamental wavelength at 1064 nm, and additional emissions at 532 and 355 nm using harmonic generators (see Table 1). The radiation is collected by a 40 cm-diameter Cassegranian telescope and then split into several detection branches. Due to the instrument setup, the incomplete overlap between the emitted laser and the telescope field of view limits the lowest possible detection height to 500 m [20,21]. A full description of the instrument before the implementation of the rotational Raman channel can be found in [22–25].

The detection branch modified for the present study was the ultraviolet (UV) part. In the previous configuration, the received beam was split by means of dichroic mirrors (DM) into three channels. The signal of each channel was then cleaned with interference filters. The first channel corresponded to the elastic signal at 355 nm, and the second and third ones were for the VR-shifted signals at 386.1 nm (for N₂) and at 407.4 nm (for water vapor).

The 386.1 nm interference filter was substituted by a double filter centered in 353.9 nm. With this filter, it was possible to detect some lines of the rotational Raman spectra of N₂ and O₂. Figure 1 shows those spectral lines weighted with the corresponding number density fractions in the atmosphere (79% and 21%, respectively) for a laser wavelength of 354.75 nm and a temperature of 300 K. The filter transmittance is also included in Fig. 1, to show the lines selected by the filter. A new configuration of dichroic mirrors was necessary in order to get enough

Table 1. Technical details of some optical elements of MULHACEN emitter system and UV detection branch

Laser source	
Emitted wavelengths, nm (Pulse duration energy, mJ)	355 (60), 532 (65) and 1064 (110)
Pulse duration, ns	8
Repetition rate, Hz	10
Optical system (UV branch)	
Interference filter wavelengths, nm (FWHM, nm / T_{\max} , %)	354.8 (1.0/57), 353.9 (0.8/59), 407.4 (1.0/67)
Dichroic mirrors transmittance (T) or reflectance (R), % (wavelength)	
DM1	R > 99% (< 410 nm)
DM2	R > 15% (407.4 nm), T > 90% (< 360 nm)
DM3	R > 96% (353.9 nm)
DM4	R > 99% (355 nm)

intense signals for all channels. With this new setup (Fig. 2), a total transmittance of almost 90% was achieved for the RR channel, without losing elastic and water vapor channels signals. A detailed description of the interference filters, dichroic mirrors and of the emission system is presented in Table 1.

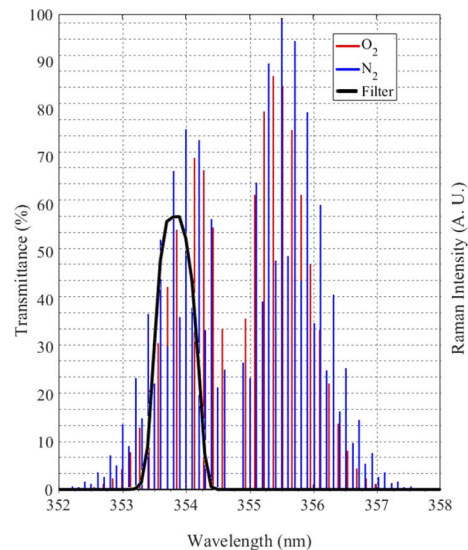


Fig. 1. Rotational Raman spectral lines (intensity in arbitrary units) of molecular oxygen (red line) and nitrogen (blue line) at 300 K, together with interference filter transmittance (black line).

Elastic and Raman lidar signals are used for the retrieval of aerosol optical properties, but several corrections (such as background noise subtraction) are applied as signal pre-processing before any retrieval algorithm. This pre-processing is standardized and validated by EARLINET-ACTRIS network [26].

The algorithm for the retrieval of aerosol extinction (α^a) and backscatter (β^a) coefficient using elastic and Raman lidar signals was first shown by [27] and then reviewed by [28,29]. In this review, the temperature dependence of the Raman scattering is shown to be important under certain conditions. In this paper, this effect is neglected after taking into account the uncertainty

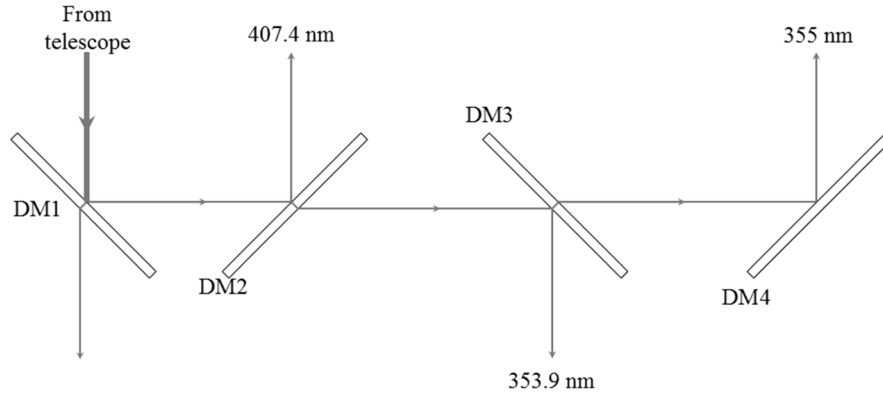


Fig. 2. Configuration of the UV detection branch of MULHACEN lidar system. Optical paths are represented by arrows and dichroic mirrors (DM) with rectangles. Different wavelength values stand for the corresponding interference filters.

introduced in the optical outputs. A quantification of such effect is shown in section 3.1 in the same way as done in [10] for 532 nm. For that reason, we show here Eqs. (1) and (2) for the calculation of β^a and α^a at each altitude z , respectively, as derived by [28] and [10]:

$$\beta^a(z) \approx -\beta^m(z) + \beta^m(z_0) \cdot \frac{P_R(z_0)P_L(z)N(z)\sigma_R^{\text{eff}}(z)}{P_L(z_0)P_R(z)N(z_0)\sigma_R^{\text{eff}}(z_0)} \quad (1)$$

$$\alpha^a(z) = \frac{\frac{d}{dz} \ln \left(\frac{N(z)}{P_R(z) \cdot z^2} \right) + \frac{d}{dz} \ln \sigma_R^{\text{eff}}(z) - \alpha_L^m(z) - \alpha_R^m(z)}{1 + \left(\frac{\lambda_L}{\lambda_R} \right)^{AE_\alpha}} \approx \frac{1}{2} \frac{d}{dz} \ln \left(\frac{N(z)}{P_R(z) \cdot z^2} \right) + \frac{1}{2} \frac{d}{dz} \ln \sigma_R^{\text{eff}}(z) - \alpha^m(z) \quad (2)$$

where the superscripts “ m ” and “ a ” indicate molecular and aerosol components of the coefficients, the subscripts “ L ” and “ R ” indicate the elastic and Raman received signals, P stands for the power of the backscattered signal, N is the molecular density, and z_0 is the reference height, chosen so that $\beta^a(z_0)$ is negligible compared to $\beta^m(z_0)$. The factor σ_R^{eff} is the effective Raman backscattering cross section:

$$\sigma_{RR}^{\text{eff}} = \int_{\Delta\lambda} \frac{d\sigma_L^m(\lambda, T)}{d\lambda} \xi_R(\lambda) d\lambda \quad (3)$$

where σ_L^m refer to the sum of all lines contributing to the molecular differential cross section, and $\xi_R(\lambda)$ is the spectral transmission of the Raman filter. The factor σ_R^{eff} is a temperature-dependent factor, whose importance is evaluated in section 3.1.

The approximation done in Eq. (2) is possible due to the small difference between elastic (λ_L) and Raman (λ_R) wavelengths, what means that $\left(\frac{\lambda_L}{\lambda_R} \right)^{AE_\alpha} \approx 1$ independently of the assumed particle extinction-related Angström Exponent (AE_α).

3. Error estimation and assessment of signal quality

In this section, three main error sources are analyzed in order to assess their effect on the uncertainty of the retrieved aerosol optical properties.

3.1. Systematic error due to temperature dependence

In Eqs. (1) and (2), the terms $\frac{\sigma_{RR}^{\text{eff}}(z)}{\sigma_{RR}^{\text{eff}}(z_0)}$ (hereinafter denoted as X) and $\Delta\alpha = \frac{1}{2} \frac{d}{dz} \ln \sigma_{RR}^{\text{eff}}(z)$ depend on the effective differential cross section of the atmosphere (that contains the contribution of the individual RR lines of N_2 and O_2). Since the intensity of these lines are temperature-dependent, the retrieved α^a and β^a profiles present a systematic error that could be significant if the temperature gradient with altitude is strong. This effect does not appear for vibrational Raman scattering, where both terms $X(z)$ and $\Delta\alpha$ can be assumed to be 1 and 0, respectively.

Authors in [10] showed that this temperature effect is small for an emission at 532.12 nm and a pure-rotational Raman filter selecting a certain spectral range. They obtained a relative error in aerosol backscatter coefficient below 1%, and absolute error of aerosol extinction coefficient below 2 Mm^{-1} for heights up to 10000 m. A similar procedure has been applied in the present work for a laser line at 354.75 nm and the transmittance of the implemented RR interference filter (described in section 2). For calculation of σ_{RR}^{eff} at different temperatures, we replaced the integral in Eq. (3) by the sum of individual RR lines of N_2 and O_2 calculated in accordance with [30] and weighted with the corresponding number density fractions in the atmosphere and the filter transmission curve (see Fig. 1). More details on the equations used to calculate the cross sections can be found in [10] or in [30]. We selected a temperature range of 230-300 K for the calculations, corresponding to heights up to around 10000 m. The temperature dependence was transformed into height dependence using 1976 US Standard Atmosphere model [31].

For β^a , the relative error (ε_β) introduced if temperature dependence is neglected can be calculated from Eq. (1) as $\varepsilon_\beta = \frac{\beta^a - \beta^a_{X=1}}{\beta^a}$, obtaining for high aerosol loads ($\beta^a \gg \beta^m$) that $\varepsilon_\beta \approx \frac{X-1}{X}$. We calculated this ε_β with respect to the temperature at the reference height of 10000 m, using transmittance of our interference filter and temperatures varying in the range 230-300 K (or heights from 0 to 10000 m according to 1976 US Standard Atmosphere). The results are plotted in Fig. 3(a), together with the used temperature profile, and it is observed that the error due to temperature effect can be up to 4% near the ground. Therefore, it can be concluded that we can neglect the temperature dependence for β^a calculation, introducing an additional uncertainty of less than 4% for reference height up to 10000 m.

The absolute error introduced in α^a if temperature dependence is neglected can be calculated according to Eq. (2) as $\Delta\alpha = \frac{1}{2} \frac{d}{dz} \ln \sigma_{RR}^{\text{eff}}(z)$, using the same σ_{RR}^{eff} variation with height as calculated for β^a . The results of this simulation together with the used temperature profile are shown in Fig. 3(b), where we can see an always negative contribution up to -1.6 Mm^{-1} . This means that the uncertainty introduced by neglecting this term is less than 2% for $\alpha^a > 80 \text{ Mm}^{-1}$.

3.2. Random errors due to temporal averaging and inversion algorithm

Statistical error in lidar analyses is mainly due to signal detection noises and to operational procedures such signal averaging [1,32]. Moreover, there is error propagation due to the application of the algorithm for the inversion of particle optical properties, and thus the analytical calculation of the uncertainties becomes very complex.

The usual technique to assess for this statistical error is based on Monte Carlo method, extracting new random lidar signals following a certain probability distribution with the measured mean and standard deviation. Then, a set of solutions are calculated with the same inversion algorithm from the generated signals, and the standard deviation is taken as the statistical error. This technique is accepted and systematically applied in EARLINET [33].

3.3. Elastic crosstalk avoidance

Another possible error source is the measurement of some elastic signal by the detector at the RR channel. This is known as elastic crosstalk, and it could appear in our system due to the close RR and elastic wavelengths, and the bandwidth of the interference filters. This effect has been tested

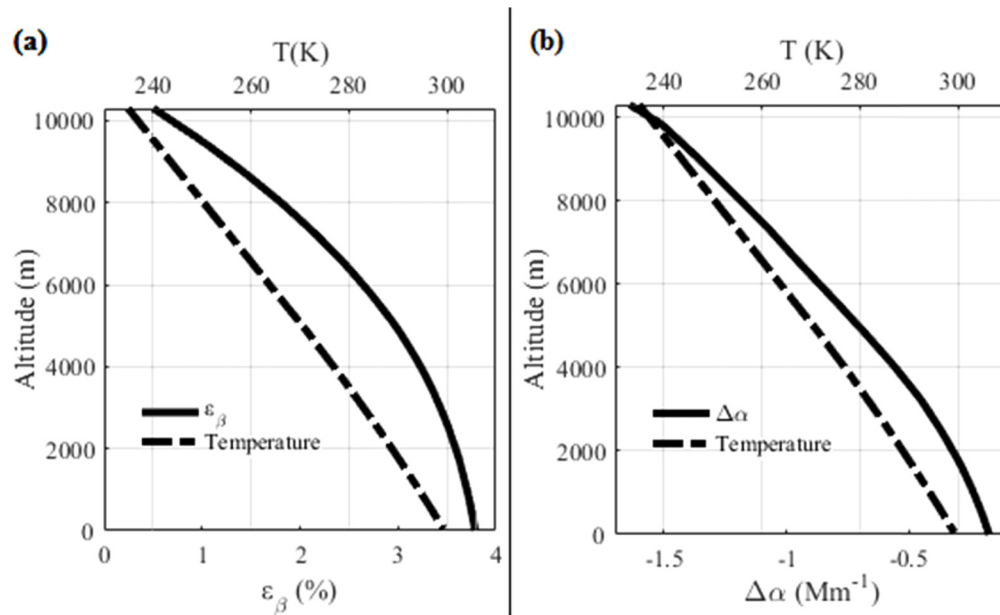


Fig. 3. (a) Relative error in β^{α} and (b) absolute error in α^{α} , due to temperature variations with altitude, using 1976 US Standard Atmosphere [31] temperature profile.

by analyzing both signals under cloudy conditions, when the elastic signal is very strong. In Fig. 4, the scattering ratio of the elastic signal, and the elastic and RR range-corrected signals (RCS) measured in an example of such test are depicted, together with the modeled molecular signal. During the measurement, some aerosol load was present until 4000 m above sea level (a.s.l.), and the cloud base was at 4500 m a.s.l. The strong enhancement of the elastic signal can be observed, with scattering ratio up to 500, while the RR signal remains unperturbed. We can then be sure that the elastic crosstalk is negligible in our system even for strong elastic signals.

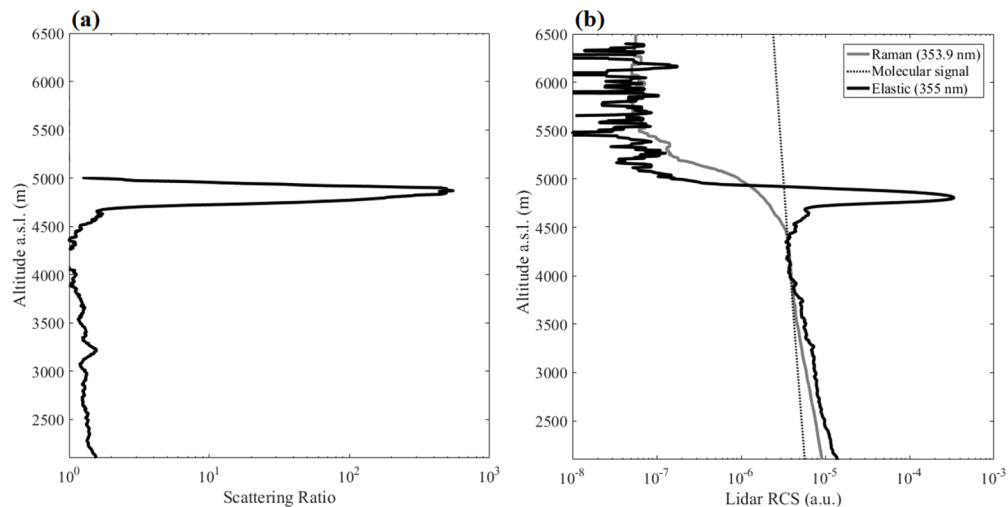


Fig. 4. (a) Elastic scattering ratio at 355 nm and (b) range-corrected elastic (355 nm, black solid line) and Raman (353.9 nm, grey solid line) lidar signals in the presence of clouds; modeled molecular backscattering is indicated by dotted line.

4. Test cases

In this section we show several examples where we evaluated the performance of the new lidar setup. The examples correspond to measurements on 25th June 2018 during night and daytime. This case was selected because the aerosol load and type was the usual for Granada [34], with aerosol optical depth (AOD) around 0.35 at 440 nm and AE_{AOD} around 0.6 at 440-870 nm. We can see the evolution of the lidar RCS at 532 nm in Fig. 5(a), and of the AOD and AE_{AOD} in Fig. 5(b), measured with triple photometer CIMEL CE318-T and obtained from Level 2.0 AERONET [35] (Version 2 algorithm) during daytime and using the algorithm described in [36] during nighttime. It can be seen that the aerosol load was roughly constant during the whole day, with only a small decrease during the first hours of the night.

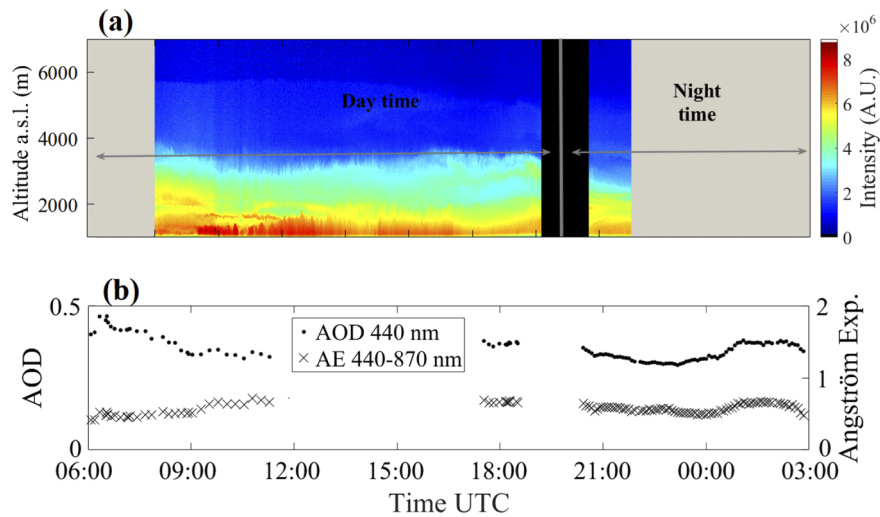


Fig. 5. (a) Time evolution of measured lidar RCS on 25th June 2018 from day to nighttime. (b) Time evolution of AOD at 440 nm and AE_{AOD} at 440-870 nm, measured with triple photometer.

With this dataset, we performed two different evaluations. Firstly, the nocturnal signals were averaged using different integration times with the aim of reducing the usual 30 min intervals. In the second part, diurnal signals were used to obtain profiles of optical properties, with a time resolution of 1 h. These profiles were then compared with the nocturnal ones, taking into account the small variations expected in the view of Fig. 5.

4.1. Nighttime profiles

Figure 6 shows the retrieved optical properties, i.e., α^a , β^a and LR^a , for the time interval from 20:34 to 21:04 UTC. The black thick lines stand for the profiles obtained from signals previously averaged for the whole period, as it was usually done for our VR lidar system. However, the increase of SNR due to RR detection allowed us to calculate the optical properties with integration times down to 1 min. The results are shown with dots in Fig. 6, and the differences observed with the 30-min-integrated profiles are up to 20% for α^a and β^a , and up to 30% for LR. The average of the 1-min-integrated optical profiles (represented as dashed lines) differ less than 10% for all profiles below 2000 m a.s.l., thus we could interpret the 1-min differences as part of the real variability of the atmosphere.

In Fig. 7, the time evolution of the α^a and β^a profiles with 1 min temporal resolution is shown. With this resolution, certain thin structures can be detected. This time resolution increase

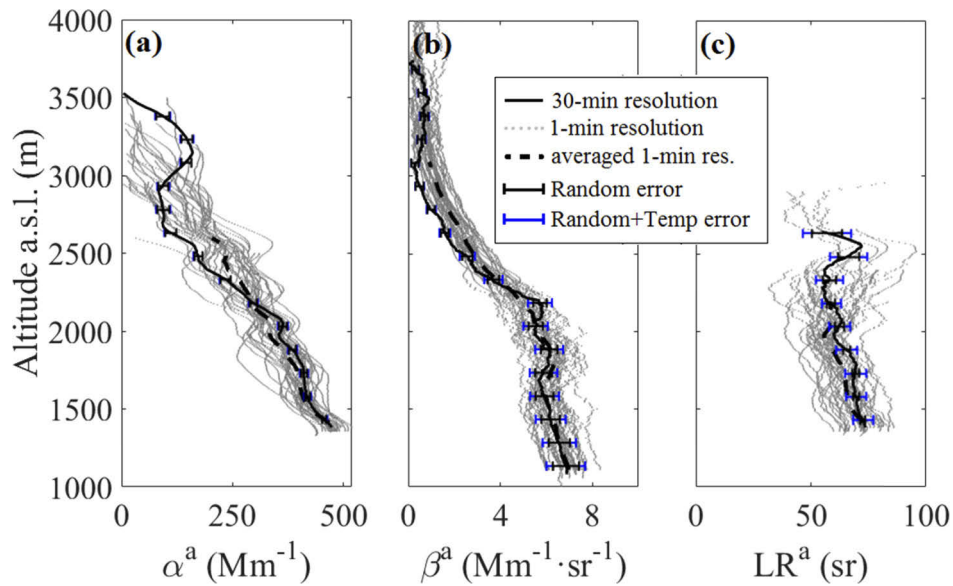


Fig. 6. Nocturnal profiles of particle backscatter (a) and extinction (b) coefficients and lidar ratio (c) for a 30-min time interval (thick lines), together with profiles obtained with 1-min resolution (dots) and their average (dashed lines). Black error bars correspond to random errors and blue error bars correspond to the temperature dependence contribution.

constitutes a clear improvement over the VR configuration, where the signals were too noisy to apply any optical retrieval algorithm for integration times less than 30 min [22,23].

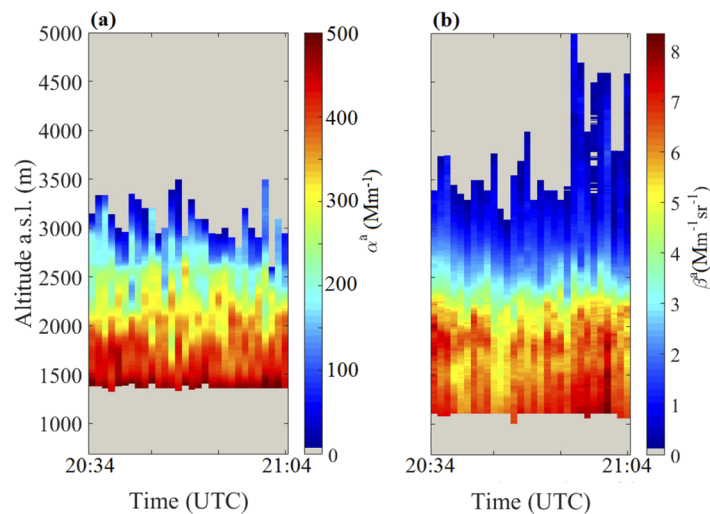


Fig. 7. Temporal evolution of particle extinction and backscatter coefficients during a nocturnal period, with 1 min resolution.

4.2. Daytime profiles

For the diurnal measurements, it was necessary the use of hourly signal averages in order to increase the SNR. The resulting elastic and RR signals allowed the retrieval of aerosol optical

properties with the Raman algorithm, a clear improvement compared with the noisy VR signals from the previous lidar configuration. The overlap function could also be calculated using the method proposed in [4]. The retrieval of such correction during daytime is an added value even to apply it to the elastic signals in Klett-Fernald inversion. In spite of this correction, the signal quality was not good enough to retrieve β^a values below 320 m (1000 m a.s.l.) and α^a values below 720 m (1400 m a.s.l.). Figure 8 and Fig. 9 show the obtained α^a and β^a profiles from 8:14 to 19:14 UTC with 1 h time resolution. The profiles do not cover the full aerosol layer (see Fig. 5(a)) due to the lower quality of the diurnal RR signal at higher altitudes. However, the results allow the observation of the aerosol layer up to 2000–3000 m a.s.l. during the whole day, in terms of optical properties.

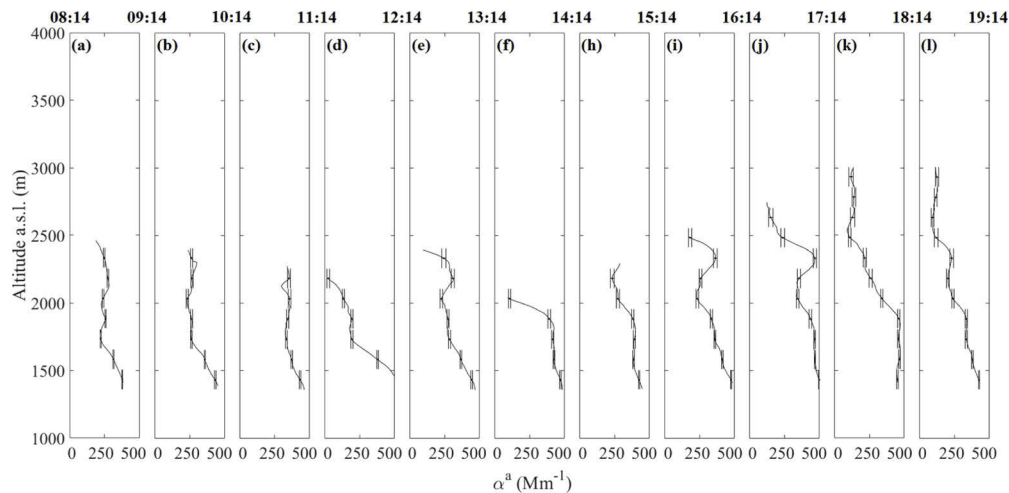


Fig. 8. Particle extinction coefficient profiles retrieved with Raman signals during daytime for 25th June 2018. Error bars correspond to random errors plus the temperature dependence contribution.

In order to check the reliability of the retrieved profiles, the elastic signal was also processed with Klett-Fernald algorithm [2,3], although only β^a can be compared using this method. For these elastic retrievals, the reference height (let us call it $z_{0,KF}$ for Klett-Fernald algorithm) was selected between 6500 and 7000 m a.s.l. to ensure that $\beta_{KF}^a(z_{0,KF}) \approx 0 \text{ m}^{-1}\text{sr}^{-1}$ (see Fig. 5). The RR signals did not have enough quality at that height, and thus the reference height for Raman method (let us call it $z_{0,R}$) was selected in the range between 2500 and 3000 m a.s.l., calibrating the retrieved β_R^a profiles so that $\beta_R^a(z_{0,R}) = \beta_{KF}^a(z_{0,KF})$. The constant LR^a values selected for Klett-Fernald algorithm were between 55 and 80 sr, selecting in each case the average of the profiles obtained with Raman method. The validation for α^a profiles was done by comparing their height-integral (AOD_{lidar}) with the AOD from AERONET (AOD_{AER}), interpolated to 355 nm.

The comparison of AOD_{lidar} versus AOD_{AER} gave us mean differences of 30%, being the minimum differences (around 15%) in the latests hours, when the background signal is smaller. These differences are reasonable, taking into account that the first 720 m of the α^a profiles were not included because of incomplete overlap effect in lidar (despite the correction applied). Additionally, the comparison between β_{KF}^a and β_R^a gave differences less than 10% at altitudes from 1000 to 2000 m a.s.l. and less than 20% for higher altitudes.

The last part of the diurnal profiling validation was to compare close retrievals, one corresponding to daytime and another to nighttime. This is the case of 18:14–19:14 UTC (daytime) and 20:34–21:04 (nighttime). We have also chosen this comparison to show an example of the measured lidar range-corrected elastic and RR signals for day and nighttime. In Fig. 10

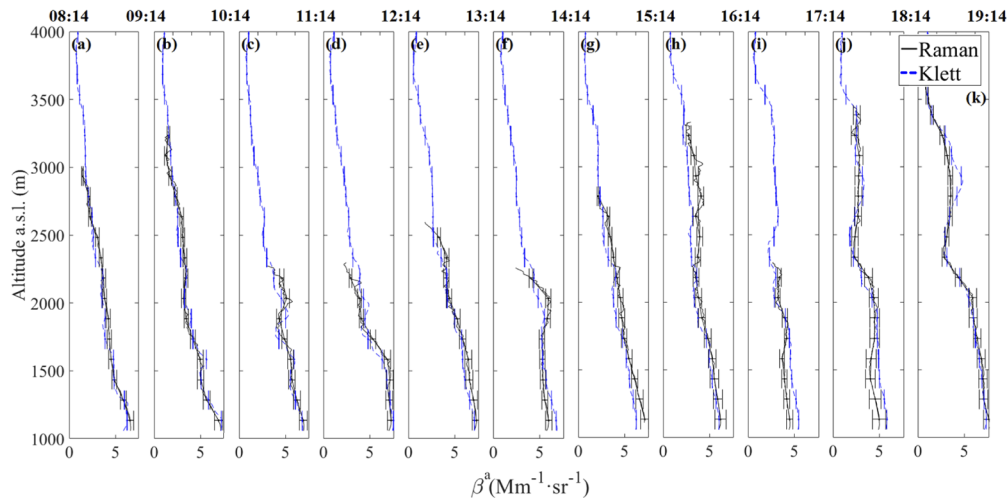


Fig. 9. Particle backscatter coefficient profiles retrieved with Raman (solid lines) and elastic (dashed lines) signals during daytime for 25th June 2018. Error bars correspond to random errors plus the temperature dependence contribution.

those signals are plotted and compared with the molecular RCS as in the ‘Rayleigh-fit’ quality assurance test that is standardized in EARLINET [37]. A moving average of 150 m and 375 m has been applied for elastic and RR signals, respectively. It can be observed in this Fig. that all signals fit with the molecular RCS for clean air (above around 5000 m a.s.l.).

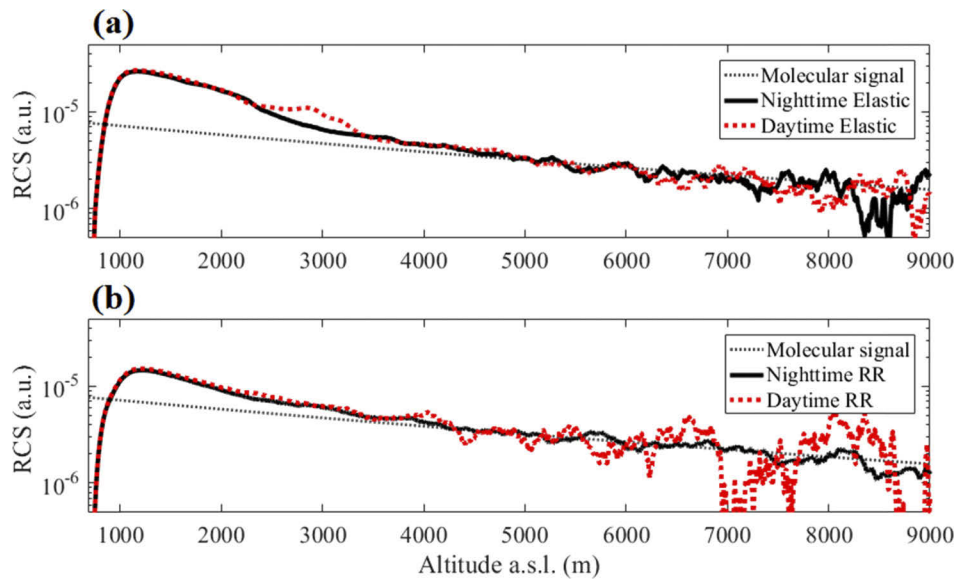


Fig. 10. Rayleigh-fit plot of daytime (18:14-19:14 h UTC) and nighttime (20:35-21:04 h UTC) lidar elastic (a) and RR (b) normalized range-corrected signals.

Optical properties, together with the calculated overlap function are shown in Fig. 11. There is an evident agreement between diurnal and nocturnal profile, except for the β^a above 2500 m a.s.l. However, it can be seen in the RCS time evolution (Fig. 5) that the aerosol load in this part of the profile actually disappears during nighttime.

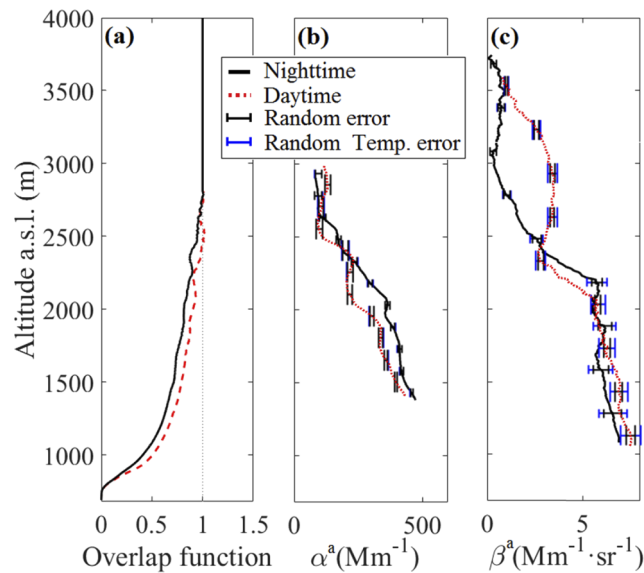


Fig. 11. (a) Overlap function, (b) particle extinction coefficient and (c) particle backscatter coefficient retrieved with RR signals during two close intervals for 25th June 2018. Black, solid lines stand for daytime profiles (18:14-19:14 h UTC) and red, dotted lines stand for nighttime profiles (20:35-21:04 h UTC). Black error bars correspond to random errors and blue error bars correspond to the temperature dependence contribution.

5. Summary and conclusions

A new setup has been implemented in the already existing Raman lidar MULHACEN at Granada station. This system used to measure vibrational Raman signals of molecules for the emission wavelengths of 355 and 532 nm. With few and simple instrumental modifications, a new interference filter has been installed in order to measure rotational Raman signal at 353.9 nm (corresponding to emission at 355 nm). The main advantages of measuring pure rotational Raman signals are the enhanced SNR and the negligible wavelength shift between elastic and Raman returns.

With this upgrade, MULHACEN is now able to provide improved measurements. These new measurements have been proved to have enough quality to obtain particle backscatter and extinction coefficient profiles during the daytime (with a time resolution of 1 h) and during nighttime (with an improved time resolution up to 1 min). We assessed the different error sources with the conclusion that the only significant uncertainty that has to be added to the statistical uncertainty is less than 2% and 4% for α^a and β^a , respectively, due to the temperature dependence of the signals.

We compared diurnal retrievals under typical aerosol load conditions, obtaining mean differences less than 30% with photometer retrievals (without considering the incomplete overlap region for lidar) and less than 20% with elastic retrievals. As an added value, we were able to calculate the correction for the incomplete overlap (overlap function) during daytime. Nocturnal retrievals with 1-min time resolution showed to reflect the variability of the atmosphere without losing the quality of the usual 30-min-averaged profiles.

Funding

Ministerio de Educación, Cultura y Deporte (FPU14/03684); Ministerio de Economía y Competitividad (CGL2016-81092-R, CGL2017-83538-C3-1-R, CGL2017-90884-REDT); Horizon 2020

Framework Programme (654109); Universidad de Granada (Excellence Units Program, Plan Propio, Programa 9, Convocatoria 2013); H2020 Marie Skłodowska-Curie Actions (754446); Russian Science Foundation (16-17-10241); Departamento Administrativo de Ciencia, Tecnología e Innovación (COLCIENCIAS) (Doctorado Nacional - 647); Universidad de Granada (Plan Propio, Programa 7, Convocatoria 2019).

Acknowledgments

The authors thankfully acknowledge the FEDER program for the instrumentation used in this work and the University of Granada that supported this study through the Excellence Units Program. The authors acknowledge the members of GFAT team from University of Granada for their work in instrument operation, measurement gathering and data analysis. We also express gratitude to B. Holben and the AERONET team for the use of the retrievals and data availability. Appreciation is also due to GOA-UVA team for photometer calibrations with particular mention of Dr. África Barreto for nocturnal *AOD* data processing and Dr. Roberto Román for the data availability.

Disclosures

The authors declare no conflicts of interest.

References

1. A. Ansmann, M. Riebesell, U. Wandinger, C. Weitkamp, E. Voss, W. Lahmann, and W. Michaelis, "Combined raman elastic-backscatter LIDAR for vertical profiling of moisture, aerosol extinction, backscatter, and LIDAR ratio," *Appl. Phys. B: Photophys. Laser Chem.* **55**(1), 18–28 (1992).
2. J. D. Klett, "Stable analytical inversion solution for processing lidar returns," *Appl. Opt.* **20**(2), 211–220 (1981).
3. F. G. Fernald, "Analysis of atmospheric lidar observations: some comments," *Appl. Opt.* **23**(5), 652–653 (1984).
4. U. Wandinger and A. Ansmann, "Experimental determination of the lidar overlap profile with Raman lidar," *Appl. Opt.* **41**(3), 511–514 (2002).
5. G. Pappalardo, A. Amodeo, A. Apituley, A. Comeron, V. Freudenthaler, H. Linné, A. Ansmann, J. Bösenberg, G. D'Amico, I. Mattis, L. Mona, U. Wandinger, V. Amiridis, L. Alados-Arboledas, D. Nicolae, and M. Wiegner, "EARLINET: Towards an advanced sustainable European aerosol lidar network," *Atmos. Meas. Tech.* **7**(8), 2389–2409 (2014).
6. J. C. Antuña-Marrero, E. Landulfo, R. Estevan, B. Barja, A. Robock, E. Wolfram, P. Ristori, B. Clemesha, F. Zaratti, R. Forno, E. Armandillo, ÁE Bastidas, ÁM De Frutos Baraja, D. N. Whiteman, E. Quel, H. M. J. Barbosa, F. Lopes, E. Montilla-Rosero, and J. L. Guerrero-Rascado, "LALINET: The first Latin American-born regional atmospheric observational network," *Bull. Am. Meteorol. Soc.* **98**(6), 1255–1275 (2017).
7. J. L. Guerrero-Rascado, E. Landulfo, J. C. Antuña, H. de Melo Jorge Barbosa, B. Barja, ÁE Bastidas, A. E. Bedoya, R. F. da Costa, R. Estevan, R. Forno, D. A. Gouveia, C. Jiménez, E. G. Larroza, F. J. da Silva Lopes, E. Montilla-Rosero, G. de Arruda Moreira, W. M. Nakaema, D. Nisperuza, D. Alegria, M. Múnera, L. Otero, S. Papandrea, J. V. Pallota, E. Pawelko, E. J. Quel, P. Ristori, P. F. Rodrigues, J. Salvador, M. F. Sánchez, and A. Silva, "Latin American Lidar Network (LALINET) for aerosol research: Diagnosis on network instrumentation," *J. Atmos. Sol.-Terr. Phys.* **138-139**, 112–120 (2016).
8. J. E. M. Goldsmith, F. H. Blair, S. E. Bisson, and D. D. Turner, "Turn-key Raman lidar for profiling atmospheric water vapor, clouds, and aerosols," *Appl. Opt.* **37**(21), 4979–4990 (1998).
9. A. Ansmann, U. Wandinger, M. Riebesell, C. Weitkamp, and W. Michaelis, "Independent measurement of extinction and backscatter profiles in cirrus clouds by using a combined Raman elastic-backscatter lidar," *Appl. Opt.* **31**(33), 7113–7131 (1992).
10. I. Veselovskii, D. N. Whiteman, M. Korenskiy, A. Suvorina, and D. Perez-Ramirez, "Use of rotational Raman measurements in multiwavelength aerosol lidar for evaluation of particle backscattering and extinction," *Atmos. Meas. Tech.* **8**(10), 4111–4122 (2015).
11. Y. Arshinov, S. Bobrovnikov, I. Serikov, A. Ansmann, U. Wandinger, D. Althausen, I. Mattis, and D. Müller, "Daytime operation of a pure rotational Raman lidar by use of a Fabry–Perot interferometer," *Appl. Opt.* **44**(17), 3593–3603 (2005).
12. J. Zeyn, W. Lahmann, and C. Weitkamp, "Remote daytime measurements of tropospheric temperature profiles with a rotational Raman lidar," *Opt. Lett.* **21**(16), 1301 (1996).
13. G. Vaughan, D. P. Wareing, S. J. Pepler, L. Thomas, and V. Mitev, "Atmospheric temperature measurements made by rotational Raman scattering," *Appl. Opt.* **32**(15), 2758–2764 (1993).

14. P. Di Girolamo, R. Marchese, D. N. Whiteman, and B. B. Demoz, "Rotational Raman Lidar measurements of atmospheric temperature in the UV," *Geophys. Res. Lett.* **31**(23), L01106 (2004).
15. D. Kim and H. Cha, "Rotational Raman Lidar: Design and Performance Test of Meteorological Parameters (Aerosol Backscattering Coefficients and Temperature)," *J. Korean Phys. Soc.* **51**(91), 352–357 (2007).
16. H. Chen, S. Chen, Y. Zhang, P. Guo, H. Chen, and B. Chen, "Robust calibration method for pure rotational Raman lidar temperature measurement," *Opt. Express* **23**(16), 21232–21242 (2015).
17. D. Wu, Z. Wang, P. Wechsler, N. Mahon, M. Deng, B. Glover, M. Burkhart, W. Kuestner, and B. Heesen, "Airborne compact rotational Raman lidar for temperature measurement," *Opt. Express* **24**(18), A1210–A1223 (2016).
18. P. Di Girolamo, A. Behrendt, and V. Wulfmeyer, "Spaceborne profiling of atmospheric temperature and particle extinction with pure rotational Raman lidar and of relative humidity in combination with differential absorption lidar: performance simulations," *Appl. Opt.* **45**(11), 2474–2494 (2006).
19. M. Haarig, R. Engelmann, A. Ansmann, I. Veselovskii, D. N. Whiteman, and D. Althausen, "1064 nm rotational Raman lidar for particle extinction and lidar-ratio profiling: Cirrus case study," *Atmos. Meas. Tech.* **9**(9), 4269–4278 (2016).
20. J. L. Guerrero-Rascado, M. J. Costa, D. Bortoli, A. M. Silva, H. Lyamani, and L. Alados-Arboledas, "Infrared lidar overlap function: an experimental determination," *Opt. Express* **18**(19), 20350–20359 (2010).
21. F. Navas-Guzmán, J. L. Guerrero-Rascado, and L. Alados-Arboledas, "Retrieval of the lidar overlap function using Raman signals," *Óptica Pura y Apl.* **44**, 71–75 (2011).
22. J. L. Guerrero-Rascado, B. Ruiz, and L. Alados-Arboledas, "Multi-spectral Lidar characterization of the vertical structure of Saharan dust aerosol over southern Spain," *Atmos. Environ.* **42**(11), 2668–2681 (2008).
23. J. L. Guerrero-Rascado, F. J. Olmo, I. Avilés-Rodríguez, F. Navas-Guzmán, D. Pérez-Ramírez, H. Lyamani, and L. A. Arboledas, "Extreme saharan dust event over the southern iberian peninsula in september 2007: Active and passive remote sensing from surface and satellite," *Atmos. Chem. Phys.* **9**(21), 8453–8469 (2009).
24. F. Navas-Guzmán, J. A. Bravo-Aranda, J. L. Guerrero-Rascado, M. J. Granados-Muñoz, and L. Alados-Arboledas, "Statistical analysis of aerosol optical properties retrieved by Raman lidar over Southeastern Spain," *Tellus B* **65**(1), 21234 (2013).
25. J. A. Bravo-Aranda, F. Navas-Guzmán, J. L. Guerrero-Rascado, D. Pérez-Ramírez, M. J. Granados-Muñoz, and L. Alados-Arboledas, "Analysis of lidar depolarization calibration procedure and application to the atmospheric aerosol characterization," *Int. J. Remote Sens.* **34**(9–10), 3543–3560 (2013).
26. G. D'Amico, A. Amodeo, I. Mattis, V. Freudenthaler, and G. Pappalardo, "EARLINET Single Calculus Chain - technical - Part 1: Pre-processing of raw lidar data," *Atmos. Meas. Tech.* **9**(2), 491–507 (2016).
27. A. Ansmann, M. Riebesell, and C. Weitkamp, "Measurement of atmospheric aerosol extinction profiles with a Raman lidar," *Opt. Lett.* **15**(13), 746–748 (1990).
28. D. N. Whiteman, "Examination of the traditional Raman lidar technique I Evaluating the temperature-dependent lidar equations," *Appl. Opt.* **42**(15), 2571–2592 (2003).
29. D. N. Whiteman, "Examination of the traditional Raman lidar technique II Evaluating the ratios for water vapor and aerosols," *Appl. Opt.* **42**(15), 2593–2608 (2003).
30. C. M. Penney, R. L. St. Peters, and M. Lapp, "Absolute rotational Raman cross sections for N₂, O₂, and CO₂," *J. Opt. Soc. Am.* **64**(5), 712–716 (1974).
31. U. S. C. on E. to the S. Atmosphere, *U.S. Standard Atmosphere* (National Oceanic and Atmospheric Administration, 1976).
32. J. Bösenberg, "Ground-based differential absorption lidar for water-vapor and temperature profiling: methodology," *Appl. Opt.* **37**(18), 3845–3860 (1998).
33. G. Pappalardo, A. Amodeo, M. Pandolfi, U. Wandinger, A. Ansmann, J. Bösenberg, V. Matthias, V. Amiridis, F. De Tomasi, M. Frioud, M. Iarlori, L. Komguem, A. Papayannis, F. Rocadenbosch, and X. Wang, "Aerosol lidar intercomparison in the framework of the EARLINET project 3 Raman lidar algorithm for aerosol extinction, backscatter, and lidar ratio," *Appl. Opt.* **43**(28), 5370–5385 (2004).
34. H. Lyamani, F. J. Olmo, and L. Alados-Arboledas, "Physical and optical properties of aerosols over an urban location in Spain: Seasonal and diurnal variability," *Atmos. Chem. Phys.* **10**(1), 239–254 (2010).
35. B. N. Holben, T. F. Eck, I. Slutsker, D. Tanré, J. P. Buis, A. Setzer, E. Vermote, J. A. Reagan, Y. J. Kaufman, T. Nakajima, F. Lavenue, I. Jankowiak, and A. Smirnov, "AERONET - A federated instrument network and data archive for aerosol characterization," *Remote Sens. Environ.* **66**(1), 1–16 (1998).
36. Á Barreto, E. Cuevas, M. J. Granados-Muñoz, L. Alados-Arboledas, P. M. Romero, J. Gröbner, N. Kouremeti, A. F. Almansa, T. Stone, C. Toledano, R. Román, M. Sorokin, B. Holben, M. Canini, and M. Yela, "The new sun-sky-lunar Cimel CE318-T multiband photometer - a comprehensive performance evaluation," *Atmos. Meas. Tech.* **9**(2), 631–654 (2016).
37. V. Freudenthaler, H. Linné, A. Chaikovski, D. Rabus, and S. Groß, "EARLINET lidar quality assurance tools," *Atmos. Meas. Tech. Discuss.* (2018).